

Observation of Orbital-Selective Band Reconstruction in an Anisotropic Antiferromagnetic Kagome Metal TbTi_3Bi_4

Renjie Zhang^{1,2,3*}, Bocheng Yu^{4*}, Hengxin Tan^{5*}, Yiwei Cheng^{6,1*}, Alfred Zong⁷, Quanxin Hu¹, Xuezhi Chen^{6,1}, Yudong Hu¹, Chengnuo Meng⁶, Junchao Ren⁶, Junqin Li⁶, Zhenhua Chen⁶, Zhengtai Liu⁶, Mao Ye⁶, Makoto Hashimoto⁸, Donghui Lu⁸, Shifeng Jin^{2,3}, Binghai Yan⁵, Ziqiang Wang⁹, Tian Shang^{4†}, Yaobo Huang^{6‡}, Baiqing Lv^{1,10,11§}, Hong Ding^{1,12,13}

¹*Tsung-Dao Lee Institute, Shanghai Jiao Tong University, Shanghai 200240, China*

²*Beijing National Laboratory for Condensed Matter Physics and Institute of Physics, Chinese Academy of Sciences, Beijing, 100190, China*

³*University of Chinese Academy of Sciences, Beijing 100049, China*

⁴*Key Laboratory of Polar Materials and Devices (MOE), School of Physics and Electronic Science, East China Normal University, Shanghai 200241, China*

⁵*Department of Condensed Matter Physics, Weizmann Institute of Science, Rehovot 7610001, Israel*

⁶*Shanghai Synchrotron Radiation Facility, Shanghai Advanced Research Institute, Chinese Academy of Sciences, 201204 Shanghai, China*

⁷*Departments of Physics and of Applied Physics, Stanford University, Stanford, CA 94305, USA*

⁸*Stanford Synchrotron Radiation Lightsource, SLAC National Accelerator Laboratory, Menlo Park, California 94025, USA*

⁹*Department of Physics, Boston College, Chestnut Hill, Massachusetts 02467, USA*

¹⁰*School of Physics and Astronomy, Shanghai Jiao Tong University, Shanghai 200240, China*

¹¹*Zhangjiang Institute for Advanced Study, Shanghai Jiao Tong University, Shanghai 200240, China*

¹²*Hefei National Laboratory, Hefei 230088, China*

¹³*New Cornerstone Science Laboratory, Shanghai 201210, China*

* These authors contributed equally to this work

† tshang@phy.ecnu.edu.cn

‡ yaobohuang@sari.ac.cn

§ baiqing@sjtu.edu.cn

ABSTRACT

Orbital selectivity is pivotal in dictating the phase diagrams of multiorbital systems, with prominent examples including the orbital-selective Mott phase and superconductivity, etc. The intercalation of anisotropic layers represents an effective method for enhancing orbital selectivity and, thereby shaping the low-energy physics of multiorbital systems. Despite its potential, related experimental studies remain limited. In this work, we systematically examine the interplay between orbital selectivity and magnetism in the newly discovered anisotropic kagome TbTi_3Bi_4 single crystal, and report a unidirectional, orbital-selective band reconstruction within the antiferromagnetic (AFM) state. By combining soft X-ray and vacuum ultraviolet angle-resolved photoemission spectroscopy (ARPES) measurements with orbital-resolved density functional theory (DFT) calculations, we identify that the band reconstruction is a manifestation of the AFM order, driven by a $1/3 a^*$ nesting instability of the intercalated Tb

$5d_{xz}$ orbitals. Such an orbital-selective modulation leads the unusual momentum-dependent band folding and the emergence of symmetry-protected Dirac cones only at the \bar{M}_1 point. More importantly, the discovery of orbital-selective 3×1 AFM order offers crucial insights into the underlying mechanism of the fractional magnetization plateau in this Kagome AFM metal. Our findings not only underscore the essential role of both conducting and localized electrons in determining the magnetic orders of $LnTi_3Bi_4$ ($Ln =$ Lanthanide) kagome metals but also offer a pathway for manipulating magnetism through selective control of anisotropic electronic structures.

INTRODUCTION

In multiorbital systems, the interplay among different orbitals gives rise to a diverse range of quantum phases and emergent phenomena [1–4]. Orbital-selectivity, a key feature of these systems, links specific orbitals to certain orders and quantum phases [3–5], including charge density wave (CDW), nematicity, and superconductivity. A crucial aspect of orbital selectivity is its connection with intrinsic anisotropy. For example, in transition metal dichalcogenides and tetrachalcogenides [6–9], d -orbitals undergo orbital-selective reconstruction within the CDW states, where the resulting orbital textures are closely related to the anisotropy. Similarly, in cuprates, the highly anisotropic stripe phase is associated with distinct behaviors of the $2p_x$ and $2p_y$ orbitals of oxygen [10,11]. For nematicity in the iron-based superconductors, orbital-selective occupancy of electronic states is proposed to account for the orbital orders, resulting in electronic and structural anisotropies [4,12]. In the context of superconductivity, the orbital-selective pairings have been proposed to account for the anisotropic superconducting gap across different orbitals [13,14].

The above examples not only highlight the intricate role of orbital-selectivity in determining the anisotropic correlated quantum phase, but also suggest an effective knob for manipulating the orbital characters through engineering anisotropic structures. Intuitively, introducing anisotropic structures—such as by intercalating layers—could modulate orbital distribution within the electronic structure, potentially enhancing orbital selectivity. More specifically, the anisotropic, low-dimensional Fermi surface that arises from selective orbitals might foster new correlated phases through mechanisms like Fermi surface nesting. As a result, it is anticipated that various correlated phases, including CDW and superconductivity, could emerge in anisotropic systems where orbital selectivity is significant [8,9,14]. However, the exploration of orbital selectivity and its correlation with other correlated quantum phases—especially magnetism—through the engineering of anisotropic structures, remains a relatively uncharted territory.

To understand the intricate relationship between orbital selectivity, anisotropy, and magnetic orders, we focus on a recently discovered kagome magnet, $TbTi_3Bi_4$, featuring double adjacent kagome layers interwoven with 1D zigzag chains of Tb atoms [15–17]. The unique combination of magnetic rare earth ions ($4f$ and $5d$ orbitals) and kagome layers (Ti $3d$ and Bi $6p$ orbitals), positions this family of compounds as a promising platform for exploring the interplay between orbital selectivity and anisotropy. Our systematic ARPES measurements reveal a highly anisotropic electronic structure in the normal state, along with a unidirectional $1/3 a^*$ orbital-selective band reconstruction in the AFM

state. By detailed analysis of the folding bands and their temperature dependence combined with orbital-characters calculations, we attribute this band reconstruction to a quasi-1D Fermi surface-nesting instability arising from the Tb- $5d_{xz}$ orbital. Following these observations, we propose a theoretical framework linking the $1/3 a^*$ AFM phase to the unique $1/3$ magnetization plateau observed in this material. Our findings not only lay the groundwork for further exploration of orbital selectivity and magnetism in similar kagome magnets but also pave the way for tuning magnetism through the control of orbital selectivity.

RESULTS

TbTi₃Bi₄ crystallizes in space group *Fmmm* (No. 69) with lattice parameters $a = 5.8332 \text{ \AA}$, $b = 10.2792 \text{ \AA}$, and $c = 24.5883 \text{ \AA}$ [Figs. 1(a) and (b)]. It shares the same structural motif as other members in the $LnTi_3Bi_4$ family, characterized by a slightly distorted Ti double kagome layer sandwiched between Tb-Bi double layers. Notably, the Tb atoms in these Tb-Bi layers form highly anisotropic quasi-1D zigzag chains that run parallel to the a -axis. In addition, TbTi₃Bi₄ exhibits an exotic $1/3$ fractional magnetization plateau when applying the magnetic field along the zigzag chain, and showcases the topological-Hall-like features [17], suggesting the intricate interplay between the electronic structure and the magnetism.

To investigate such an interplay, we systematically performed magnetic and electrical characterizations, as well as ARPES measurements. As shown in Fig. 1(c), TbTi₃Bi₄ exhibits metallic behavior at low temperatures, with a distinct kink in the temperature-dependent electrical resistivity $\rho_{xx}(T)$ at $T_N \sim 20.4 \text{ K}$. Fig. 1(d) displays the temperature dependence of magnetization $M(T)$ collected by applying magnetic fields along three different axes. For $H//a$, a sharp peak was observed at 20.4 K in the $M(T)$, consistent with the resistivity data in Fig. 1(c), demonstrating the onset of AFM order in TbTi₃Bi₄ single crystal.

Interestingly, the AFM transition is much less pronounced for either $H//b$ or $H//c$, implying a strong magnetic anisotropy in TbTi₃Bi₄ and suggesting that the Tb moments are predominantly aligned along the a -axis, i.e., the direction of the zigzag chains. Furthermore, the field-dependent magnetization $M(H)$ curves [Fig. 1(e)] reinforce the magnetic anisotropy, identifying the a -axis as the easy axis while the b - and c -axes as the hard axes.

Uniquely, after undergoing a metamagnetic transition at $\sim 1 \text{ T}$, there is a $1/3$ magnetization plateau in the field range of approximately 1 T to 2.5 T in the $M(H)$ for $H//a$, as shown in Fig. 1(e). When the magnetic field exceeds approximately 3 T , the magnetization saturates, indicating the establishment of a forced ferromagnetic arrangement. Such metamagnetic transitions and magnetization plateau are absent for both $H//b$ and $H//c$. Magnetoresistance measurements (see Appendix A) further confirm the metamagnetic transitions observed in the $M(H)$ curves, and together with the $M(T)$ curves, they outline a rich magnetic phase diagram for TbTi₃Bi₄ (see Appendix A).

The observed highly anisotropic and intriguing magnetic properties are most likely due to the interplay between itinerant electrons and local magnetic moments of Tb $4f$ electrons. To elucidate the electronic structure of TbTi₃Bi₄, we performed density functional theory (DFT) calculations. Fig. 2 displays the calculated band dispersion at $k_z = 0$ and $k_z = \pi$ planes (defined in the 1st Brillouin zone, or BZ, same as below). The calculations reveal several characteristic features for this kagome-lattice

compound, including van Hove singularities (vHS) and flat bands. Notably, the inequivalence of the vHSs at M_1/M_2 and L_1 highlights the anisotropy in the normal-state electronic structure, a trait commonly observed in the LnTi_3Bi_4 family [18,19]. Additionally, the observation of two closely spaced flat bands below the Fermi level (E_F) reflects the existence of double kagome layers within a single unit cell were identified [19]. Due to the presence of the rotation-symmetry-breaking intercalating layers, intrinsic strain, from the anisotropic structure, makes the Dirac point away from the high-symmetry point of the bulk BZ (K_1/K_2 and H_1/H_2) [20] and thus is absent in the DFT calculation results shown along the high symmetry line.

To experimentally determine the electronic structure and understand its relationship with an intrinsic magnetic order, we continued to conduct ARPES measurements. We first mapped the Fermi surface within the $k_x - k_y$ plane [Fig. 3(a)] and along the k_z direction [Fig. 3(b)] using both vacuum ultraviolet (VUV) light and soft X-ray (Appendix C). The consistency between the VUV and soft X-ray data demonstrates that our data predominantly represent bulk states. More specifically, from Fig. 3(b), one can see that the Fermi surface along the k_z direction appears nearly non-dispersive. We interpret this as a result of both the quasi-2D nature of bands near the E_F and the k_z broadening [21].

Next, we focused on the ARPES measurements with VUV light to clarify the band structure near E_F . Starting from the center of the BZ, we identify two electron-like pockets forming two concentric circular Fermi surfaces (labeled as α and α') around $\bar{\Gamma}$ point [Fig. 3(a), (c) and (d)]. Note that the observed small splitting between α and α' is not seen in the DFT calculations (Fig. 2), and we attribute this splitting between α and α' to the surface effect caused by the self-doping of the non-neutral cleavage surface, which was commonly observed and well-studied in AV_3Sb_5 [22]. Next, we turn to the BZ corners, \bar{K}_1/\bar{K}_2 . At these points, there are point-like Fermi pockets ϵ , which is formed by the near E_F Dirac point and can be clearly resolved in Fig. 3(c), (d). In addition, a triangular hole-like Fermi surface δ is seen around \bar{K}_1/\bar{K}_2 [Fig. 3(a), (c) and (d)].

Interestingly, as we move toward the \bar{M}_1/\bar{M}_2 points, vHSs near the E_F become distinctly observable. Akin to the AV_3Sb_5 family [23–28], bands emanating from the vHSs cross the E_F and form a large γ pocket near the BZ boundary. However, the vHSs at \bar{M}_1/\bar{M}_2 are not equivalent due to the anisotropy of this material, leading to the warped Fermi surface [18,19,29,30], which deviates from the ideal nesting condition in the AV_3Sb_5 family [23–28]. This imperfect nesting between vHSs may explain the absence of CDW order in the kagome layer [25].

After the identification of the typical kagome features, our attention shifts to the characteristics of the Tb 1D zigzag chains. As shown in Fig.3(a), from the Fermi surface map in the second BZ, one can identify a quasi-1D line perpendicular to the Tb chain direction (i.e., a^* , parallel to the $\bar{\Gamma}-\bar{M}_1$ direction). Detailed analysis (see Appendix E) reveals that this 1D line is formed by two quasi-1D Fermi surfaces β and β' , denoted by red and white markers in Fig. 3(a), respectively. The β/β' bands have an electron-like dispersion parallel to the chain direction [Fig. 3 (c) and (d)]. The presence of these quasi-1D β/β' pockets, supported also by the DFT calculations (see Appendix B for details), are key features of the 1D Tb chains.

Having established the electronic structure in the normal state, we now shift our focus to the AFM state. Figs. 3(e) and (f) present the high-symmetry cuts in the AFM state. Compared with the normal-state results [Figs. 3(c) and (d)], we found that the kagome electronic features, including the vHSs, the Dirac points and the flat bands, remain largely unaffected by the AFM order. On the other hand, when

we turn our attention to the bands along the $\bar{K}_1\text{-}\bar{M}_1$ path [highlighted by the red dashed rectangles in Fig. 3(d) and (f), aligned with the zigzag chain direction], we observe clear differences, suggesting the emergence of momentum-dependent band reconstruction in the AFM state.

To better visualize the band reconstruction, we systematically compared the measured high-resolution intensity and the corresponding curvature intensity plots along both $\bar{K}_1\text{-}\bar{M}_1\text{-}\bar{K}_1$ [Figs. 4(a) and (b)] and $\bar{K}_1\text{-}\bar{M}_2\text{-}\bar{K}_2$ directions [Figs. 4(c) and (d)]. Our findings are twofold. Firstly, a distinct Dirac-cone-type crossing and some additional new states were observed along $\bar{K}_1\text{-}\bar{M}_1\text{-}\bar{K}_1$ direction below T_N , as demonstrated by the red markers in Fig. 4(b)-(ii) and the emergence of Peak 3 in Fig. 4(g). Secondly, a suppression of the band intensity is noticeable in the energy range of approximately -0.1 eV to -0.2 eV along the $\bar{M}_1\text{-}\bar{K}_1$ direction below T_N , more clearly in the curvature intensity plot [highlighted by the black rectangle in Fig. 4(b)-(i)]. In sharp contrast, despite these pronounced changes around \bar{M}_1 , there is no distinct variations along the $\bar{K}_1\text{-}\bar{M}_2\text{-}\bar{K}_2$ direction [Figs. 4(c) and (d)], underscoring the strong anisotropy and momentum dependence for the band reconstruction.

To be more precise, we extracted the dispersions of both the original bands in the normal state [indicated by grey lines in Fig. 4(a)] and the emergent Dirac bands in the AFM state [marked by red squares and diamonds in Fig. 4(b)-(ii)]. Intriguingly, these emergent bands can be folded onto the original bands by a vector $q \approx 0.36 \text{ \AA}^{-1}$ [$\sim 1/3 a^*$, $a^* = 2\pi/a$, as shown by the black arrows in Fig. 4(f)], suggesting the emergence of a density wave order associated with the vector q . The formation of this density wave order leads to hybridization gaps at some specific crossing points of the folded bands, explaining the suppression of band intensity near the region highlighted by the black rectangle [Fig. 4(b)]. Importantly, the observation of emergent Dirac point at the BZ boundary points towards the accompaniment of a topological transition in the AFM state, which calls for further study.

To further verify the band folding, we turn our attention to the electron pockets near the $\bar{\Gamma}$ point. The measured intensity plots above and below T_N along the $\bar{\Gamma}\text{-}\bar{K}_2$ directions are summarized in Fig. 5. A gap of approximately 42.9 meV was observed on the outer band around $\bar{\Gamma}$, with obvious band back-bending features [Fig. 5 (e) and (f)]. As expected, the momentum separation of the left and right sides of the gapped outer band matches well with q . These observations reaffirm the existence of density wave modulations in TbTi_3Bi_4 .

One of the predominating driving forces behind the density wave modulation is the Fermi surface nesting. In quasi-1D systems, the ideal nesting condition is often naturally present due to the prevalence of 1D Fermi surface. As demonstrated in Fig. 3(a) and Appendix E, TbTi_3Bi_4 hosts a quasi-1D Fermi surface β thanks to the intercalation of 1D Tb chains. Therefore, it's natural to link the density wave to the β Fermi surface. Indeed, from the mapped Fermi surfaces [Fig. 5(a)], one can see that the two branches of the β Fermi surface can be connected by a vector q , strongly suggesting β as the underlying driving force for the observed density waves. Meanwhile, one would expect the opening of an energy gap at the E_F for this β pocket. To this end, we performed a cut along β (see Appendix E). Comparing the AFM state with the normal state, we indeed find a gap opening of approximately 77.6 meV with respect to the E_F . These observations pin down that the anisotropic band reconstruction observed below T_N is primarily driven by the nesting of quasi-1D Fermi surface.

The dichotomy in band reconstruction between the \bar{M}_1 point and the other k -points in momentum space, especially the \bar{M}_2 point [Fig. 4(c), (d)], is surprising, as one would naively expect all bands to be reconstructed under density wave modulation. Given the multiorbital nature of TbTi_3Bi_4 ,

understanding the orbital distribution is essential for comprehending this momentum-dependent band reconstruction. First of all, as shown in Fig. 4(e) and 4(f), a comparison of the normal-state band dispersion extracted from ARPES [Fig. 4(f)] with the k_z -projected DFT calculations [Fig. 4(e)] shows that the observed folded bands mainly reside in the $k_z = \pi$ plane, suggesting that the band structure in this plane plays a crucial role for such a band folding. Collaboratively, DFT calculations reveal the presence of well-nested quasi-1D Fermi surface in the $k_z = \pi$ plane [see Fig.5(b)]. Since the band reconstruction is most pronounced in the $k_z = \pi$ plane and along the quasi-1D Fermi surface, our analysis focuses on these features. Fig. 6 and Appendix F summarize the orbital-resolved DFT results. Interestingly, though the Ti-3d orbitals dominate the near- E_F energy bands (see Appendix F), the $5d_{xz}$ orbital (x and z align with a and c axis, respectively) of Tb is closely tied to the reconstructed bands below T_N (Fig. 6), demonstrating the orbital-selective band reconstruction in the AFM state.

DISCUSSION

Taken together, our temperature-dependent ARPES results reveal orbital-selective band reconstruction, pointing towards the existence of unidirectional density wave modulation with a q vector of $1/3 a^*$. We believe that the density wave modulation originates from the AFM order for the following reasons: (1) The temperature at which the folded Dirac bands [Peak 3 in Figs. 4 (g) and (h)] appear coincides with the bulk AFM transition temperature ($T_N \sim 20.4$ K); (2) The quasi-1D Fermi surface highly related to $5d_{xz}$ orbital of magnetic Tb atoms drives the density wave instability through ideal nesting condition; (3) $4f$ orbitals of Tb, forming the AFM order, strongly couple to the $5d$ orbitals, which concentrate on the well-nested quasi-1D Fermi surface. Given the strong correlation between the band reconstruction and the bulk AFM order, we can exclude the surface effects, e.g., surface reconstruction. Furthermore, it is unlikely that a structure transition is solely responsible, since the reconstruction is observed only at specific momentum associated with the Tb- $5d_{xz}$ orbital. In contrast, a structural transition would typically result in band foldings across all the electronic bands, whereas in our case, the bands at the \bar{M}_2 and \bar{K}_1/\bar{K}_2 points are scarcely affected.

Anisotropy and orbital selectivity are critical factors influencing both band reconstruction and magnetism. In general, both the anisotropic crystal structure and the resulting orbital textures determine the orbital distribution within the band structure. Specifically, the relative orientation and spatial arrangement of intrinsically anisotropic orbital wavefunctions have a prominent effect on the overlap integrals, which directly govern the band dispersion and the associated orbital characters [6,7,9]. In our study, the anisotropy facilitates the predominance of $5d_{xz}$ orbitals in the well-nested quasi-1D Fermi surface. With a strong coupling between $5d$ and $4f$ electrons [31–34], $5d_{xz}$ itinerant electrons form spin density wave (SDW) through Fermi surface nesting and in turn induce a long-range RKKY interaction between $4f$ electrons [35–37], thus modulating local moments arrangement [31,38,39]. In the case of TbTi₃Bi₄, by combining long-range RKKY interactions with nearest-neighbor and next-nearest-neighbor short-range couplings, it is plausible that an AFM state with a $q \sim 1/3 a^*$ arises in this intercalated kagome magnet due to competing magnetic couplings. Additionally, regarding magnetism, it has been reported that orbital-selective exchange interactions are crucial in determining the magnetic properties in the lanthanide compounds. For example, in the skyrmion material Gd₂PdSi₃, the competition between Gd $5d$ ferromagnetic exchange interactions and

Gd $4f$ antiferromagnetic exchange interactions may lead to the formation of complex skyrmion spin textures [34]. This orbital-selective exchange interaction among different orbitals of lanthanide elements could explain different magnetic ground states ranging from ferromagnetism to AFM in the $LnTi_3Bi_4$ family [29,40].

More importantly, the above analysis inspires us to propose a plausible mechanism to explain the $1/3$ fractional magnetization plateau based on the $1/3 a^*$ AFM state. As illustrated in Fig. 7 (b), since the q -vector is approximately $1/3 a^*$, the possible magnetic structure should have a period of $3a$ in real space. In this model [Fig. 7 (c)], each zigzag chain constitutes of two layers of local moments. In each layer, moments are arranged as left-left-right (or right-right-left), with adjacent layers oriented oppositely. Assuming that intralayer coupling is stronger than the interlayer coupling (an alternative case is illustrated in Appendix G), an applied magnetic field exceeding H_1 first overcomes the nearest-neighbor magnetic coupling, and results in flips of all the spins in one layer to align with the adjacent layer, gaining energy through aligning majority of local moments with the external field. This transition corresponds to the $1/3$ fractional plateau. As the magnetic field surpasses H_2 , the remaining unflipped moments in two separated layers flip together [Fig. 7 (c)] or flip one by one to align with the field (if the interlayer coupling is weaker than the intralayer coupling, these two ways are close in terms of energy), leading to saturation of magnetization or $2/3$ kink, respectively. This mechanism naturally explains the $1/3$ fractional magnetization plateau observed experimentally in the $1/3 a^*$ AFM state, and also accounts for the weak kink in the magnetization curve reported recently [15–17]. It's also worth cautioning that though it's very reasonable to attribute the band reconstruction and the $1/3$ fractional plateau to the bulk 3×1 AFM state, we cannot exclude a more exotic scenario of coexisting the unidirectional 3×1 charge density wave order and the 1×1 AFM order. Looking forward, it's essential to employ neutron diffraction measurements to identify the periodicity of the AFM order.

Last but not least, we emphasize the potential complex interplay among orbital-selectivity, magnetism and charge order/lattice. First, CDW often intertwines with AFM (or SDW) in many materials. For the canonical SDW system, chromium, a CDW state with a half-period of the SDW state has been observed coexisting with SDW, and may also originate from the Fermi nesting [41]. Additionally, recent work has reported that SDW and CDW may coexist under ambient pressure and decouple with each other under high pressure in kagome metal $CsCr_3Sb_5$ [42]. In the case of $TbTi_3Bi_4$, we find a quasi-1D Fermi surface with a favorable nesting condition, which could not only promote the modulation of the AFM state through RKKY interaction, but also facilitate the formation of the CDW state through nesting. Second, magneto-elastic coupling, which describes the interaction between magnetization and lattice distortion, is ubiquitous in magnetic materials, particularly those with strong anisotropy [43,44]. As previously discussed, the easy axis of $TbTi_3Bi_4$ aligns with the zigzag chain, and prior work has highlighted the critical role of the crystal field effect in the magnetization anisotropy [15]. Therefore, it is anticipated that the magnetostriction, associated with this anisotropy, could be observable along zigzag chain in $TbTi_3Bi_4$. Furthermore, due to the direct correlation between orbital arrangement in real space and the lattice structure, magnetic orbital-selective band reconstruction of $5d_{xz}$ is expected to induce modifications in the related lattice degrees of freedom through orbital overlap between atoms. In our study, the Tb zigzag chain structure is likely to undergo modulation linked to the AFM transition. Third, as discussed earlier, Tb $5d_{xz}$ -related quasi-1D Fermi surface may determine the magnetism of $TbTi_3Bi_4$, suggesting the possibility of controlling

magnetism by selectively tuning the orbitals. For instance, uniaxial strain applied along the zigzag chain could alter the $5d_{xz}$ orbital overlap, thereby modifying the quasi-1D Fermi surface associated with this orbital. In addition, since magnetism is directly coupled to the lattice degree of freedom, strain could also modulate the magnetization through inverse magnetostriction [43,44]. This approach offers a promising avenue for controlling magnetism through selective tuning of the orbitals and lattice structure.

CONCLUSION

In conclusion, we present a comprehensive study on the electronic structure of the anisotropic kagome magnet TbTi_3Bi_4 , combining ARPES measurements with DFT calculations. Our systematic temperature-dependent investigation in momentum space reveals a unidirectional $1/3 a^*$ band folding in the AFM state. Notably, this band folding results in the formation of a crystal symmetry-protected Dirac cone at the BZ boundary, hinting at the realization of magnetic-order-induced topological transition. The combination of ARPES data and DFT calculations suggests that the nesting of the quasi-1D Fermi surface drives this band folding. Very importantly, our orbital-resolved DFT calculations demonstrate a direct correlation between the Tb $5d_{xz}$ orbital and the observed surprising momentum-dependent band reconstruction in the AFM state. This orbital-selective band reconstruction underscores the need for further research into its potential role in the rich magnetic properties of TbTi_3Bi_4 and other materials in the $Ln\text{Ti}_3\text{Bi}_4$ family. Our finding provides key insights into the nature of the AFM state and the unusual fractional plateau of TbTi_3Bi_4 , and opens avenues for manipulating magnetism through the orbital-selective control of the electronic structure.

METHODS

A. Single crystal synthesis and Sample characterization

TbTi_3Bi_4 single crystals were grown using a molten Bi flux method. High purity Tb pieces (Thermo Fisher Scientific 99.9%), Ti granules (Thermo Fisher Scientific 99.99%), and Bi granules (Aladdin, 99.999%) in a ratio of 2:3:12 were loaded in an alumina crucible and sealed in a quartz ampule. Then, the quartz ampule was heated up to 1050 °C at a rate of 200 °C/h. After annealing at this temperature for more than 30 h, the ampule was slowly cooled down to 500°C at a rate of 2 °C/h. After removing the excess Bi flux using a centrifuge, single crystals with typical dimension 2 mm \times 2 mm \times 0.5 mm were obtained, which show a hexagonal shape.

The crystal structure of TbTi_3Bi_4 single crystals was checked via XRD at room temperature using an Empyrean x-ray diffractometer with Cu $K\alpha$ radiation (Panalytical). Consistent with previous results, we confirm that our TbTi_3Bi_4 crystals crystallize in a centrosymmetric cubic structure (space group $Fm\bar{3}m$, No. 69). The XRD measurements performed on a TbTi_3Bi_4 single crystal reveal a series of $(00l)$ reflections [Figure 1(b)], confirming the single-crystal nature of the TbTi_3Bi_4 sample and its c -axis is perpendicular to the crystal plane.

Magnetization and electrical transport measurements were performed in a Quantum Design

magnetic properties measurement system and physical property measurement system, respectively. For the resistivity measurements, the electric current was applied within the *ab* plane, while the magnetic field was applied along the *c* axis.

B. ARPES Measurement

ARPES measurements were performed at BL-09U and BL-03U of the Shanghai Synchrotron Radiation Facility (SSRF), and at BL 5-2 of the Stanford Synchrotron Radiation Lightsource (SSRL), all equipped with a SCIENTA Omicron DA30L analyzer. The energy resolution at BL-09U and BL-03U (SSRF) was 10 meV - 60 meV, with an angular resolution of 0.1° . The energy and angular resolutions at BL 5-2 (SSRL) were 5 meV – 20 meV and 0.1° , respectively. Samples were cleaved *in situ* and measured under a base vacuum better than 5×10^{-11} Torr.

C. DFT Calculation

Density functional theory (DFT) calculations are performed within the Vienna *ab-initio* simulation package [45]. The PBE-type generalized gradient approximation [46] is used to mimic the electronic exchange-correlation interaction. The projector augmented wave potentials with 9 valence electrons for Tb (*f* electrons are not considered), 4 valence electrons for Ti, and 5 valence electrons for Bi are employed. The crystal structure of TbTi_3Bi_4 is fully relaxed until the remaining force on all atoms is no larger than 1 meV/Å. The energy cutoff for the plane wave basis set is 250 eV. A *k*-mesh of $6 \times 6 \times 6$ is utilized to sample the reciprocal space. Spin-orbit coupling is considered for all calculations except for the structural relaxation. The Fermi surface is calculated by the wannier Hamiltonian [47] extracted from DFT calculations with the basis set composed of Tb *d*, Ti *d*, and Bi *p* orbitals.

ACKNOWLEDGEMENT

We are grateful to Chun Lin, Jianyang Ding, Jiayu Liu and Gexing Qu for their assistance in our ARPES measurements. We are also grateful to Mojun Pan for helpful discussions. B.L. acknowledges support from the Ministry of Science and Technology of China (2023YFA1407400), the National Natural Science Foundation of China (12374063), the Shanghai Natural Science Fund for Original Exploration Program (23ZR1479900), and the Cultivation Project of Shanghai Research Center for Quantum Sciences (Grant No. LZPY2024). H. D. acknowledges support from the New Cornerstone Science Foundation (No. 23H010801236), Innovation Program for Quantum Science and Technology (No. 2021ZD0302700). Y. B. H. acknowledges support by the Shanghai Committee of Science and Technology (Grant No. 23JC1403300), the Shanghai Municipal Science and Technology Major Project. Z.W. is supported by the US Department of Energy, Basic Energy Sciences Grant DE-FG02-99ER45747.

- [1] G. R. Stewart, Non-Fermi-liquid behavior in d- and f-electron metals, *Rev. Mod. Phys.* **73**, 797 (2001).

- [2] P. Gegenwart, Q. Si, and F. Steglich, Quantum criticality in heavy-fermion metals, *Nature Phys* **4**, 3 (2008).
- [3] A. Georges, L. de' Medici, and J. Mravlje, Strong Correlations from Hund's Coupling, *Annual Review of Condensed Matter Physics* **4**, 137 (2013).
- [4] R. M. Fernandes, A. I. Coldea, H. Ding, I. R. Fisher, P. J. Hirschfeld, and G. Kotliar, Iron pnictides and chalcogenides: a new paradigm for superconductivity, *Nature* **601**, 7891 (2022).
- [5] R. Yu, H. Hu, E. M. Nica, J.-X. Zhu, and Q. Si, Orbital Selectivity in Electron Correlations and Superconducting Pairing of Iron-Based Superconductors, *Front. Phys.* **9**, (2021).
- [6] T. Ritschel, J. Trinckauf, K. Koepf, B. Büchner, M. v Zimmermann, H. Berger, Y. I. Joe, P. Abbamonte, and J. Geck, Orbital textures and charge density waves in transition metal dichalcogenides, *Nature Phys* **11**, 4 (2015).
- [7] M. D. Watson, O. J. Clark, F. Mazzola, I. Marković, V. Sunko, T. K. Kim, K. Rossnagel, and P. D. C. King, Orbital- and k_z -Selective Hybridization of Se 4p and Ti 3d States in the Charge Density Wave Phase of TiSe_2 , *Phys. Rev. Lett.* **122**, 076404 (2019).
- [8] N. Mitsuishi et al., Switching of band inversion and topological surface states by charge density wave, *Nat Commun* **11**, 2466 (2020).
- [9] R. Z. Xu et al., Orbital-selective charge-density wave in TaTe_4 , *Npj Quantum Mater.* **8**, 1 (2023).
- [10] K. Fujita et al., Direct phase-sensitive identification of a d-form factor density wave in underdoped cuprates, *Proceedings of the National Academy of Sciences* **111**, E3026 (2014).
- [11] R. Comin et al., Symmetry of charge order in cuprates, *Nature Mater* **14**, 796 (2015).
- [12] R. M. Fernandes, A. V. Chubukov, and J. Schmalian, What drives nematic order in iron-based superconductors?, *Nature Phys* **10**, 2 (2014).
- [13] R. Yu, J.-X. Zhu, and Q. Si, Orbital-selective superconductivity, gap anisotropy, and spin resonance excitations in a multiorbital t - J_1 - J_2 model for iron pnictides, *Phys. Rev. B* **89**, 024509 (2014).
- [14] P. O. Sprau, A. Kostin, A. Kreisel, A. E. Böhmer, V. Taufour, P. C. Canfield, S. Mukherjee, P. J. Hirschfeld, B. M. Andersen, and J. C. S. Davis, Discovery of orbital-selective Cooper pairing in FeSe , *Science* **357**, 75 (2017).
- [15] K. Guo, Z. Ma, H. Liu, Z. Wu, J. Wang, Y. Shi, Y. Li, and S. Jia, 1/3 and other magnetization plateaus in the quasi-one-dimensional Ising magnet TbTi_3Bi_4 with zigzag spin chain, *Phys. Rev. B* **110**, 064416 (2024).
- [16] B. R. Ortiz et al., Intricate Magnetic Landscape in Antiferromagnetic Kagome Metal TbTi_3Bi_4 and Interplay with $\text{Ln}_{2-x}\text{Ti}_{6+x}\text{Bi}_9$ (Ln: Tb...Lu) Shurikagome Metals, *Chem. Mater.* **36**, 8002 (2024).
- [17] E. Cheng et al., Giant anomalous Hall effect and band folding in a Kagome metal with mixed dimensionality, *arXiv* 2405.16831 (2024).
- [18] Z. Jiang et al., Direct observation of topological surface states in the layered kagome lattice with broken time-reversal symmetry, *arXiv* 2309.01579 (2023).
- [19] Y. Hu et al., Magnetic-coupled electronic landscape in bilayer-distorted titanium-based kagome metals, *arXiv* 2311.07747 (2023).
- [20] C. Si, Z. Sun, and F. Liu, Strain engineering of graphene: a review, *Nanoscale* **8**, 3207 (2016).
- [21] V. N. Strocov, Intrinsic accuracy in 3-dimensional photoemission band mapping, *Journal of*

Electron Spectroscopy and Related Phenomena **130**, 65 (2003).

- [22] T. Kato et al., Surface-termination-dependent electronic states in kagome superconductors AV_3Sb_5 ($A = K, Rb, Cs$) studied by micro-ARPES, *Phys. Rev. B* **107**, 245143 (2023).
- [23] Z. Liu et al., Charge-Density-Wave-Induced Bands Renormalization and Energy Gaps in a Kagome Superconductor RbV_3Sb_5 , *Phys. Rev. X* **11**, 041010 (2021).
- [24] S. Cho et al., Emergence of New van Hove Singularities in the Charge Density Wave State of a Topological Kagome Metal RbV_3Sb_5 , *Phys. Rev. Lett.* **127**, 236401 (2021).
- [25] M. Kang et al., Twofold van Hove singularity and origin of charge order in topological kagome superconductor CsV_3Sb_5 , *Nat. Phys.* **18**, 301 (2022).
- [26] Y. Hu et al., Rich nature of Van Hove singularities in Kagome superconductor CsV_3Sb_5 , *Nat Commun* **13**, 2220 (2022).
- [27] H. Luo et al., Electronic nature of charge density wave and electron-phonon coupling in kagome superconductor KV_3Sb_5 , *Nat Commun* **13**, 273 (2022).
- [28] T. Kato et al., Three-dimensional energy gap and origin of charge-density wave in kagome superconductor KV_3Sb_5 , *Commun Mater* **3**, 1 (2022).
- [29] J. Guo et al., Tunable magnetism and band structure in kagome materials $RETi_3Bi_4$ family with weak interlayer interactions, *Science Bulletin* (2024).
- [30] Z. Zheng, L. Chen, X. Ji, Y. Zhou, G. Qu, M. Hu, Y. Huang, H. Weng, T. Qian, and G. Wang, Anisotropic magnetism and band evolution induced by ferromagnetic phase transition in titanium-based kagome ferromagnet $SmTi_3Bi_4$, *Sci. China Phys. Mech. Astron.* **67**, 267411 (2024).
- [31] S. H. Liu, *Chapter 3 Electronic Structure of Rare Earth Metals*, in *Handbook on the Physics and Chemistry of Rare Earths*, Vol. 1 (Elsevier, 1978), pp. 233–335.
- [32] K. M. Döbrich, G. Bihlmayer, K. Starke, J. E. Prieto, K. Rossnagel, H. Koh, E. Rotenberg, S. Blügel, and G. Kaindl, Electronic band structure and Fermi surface of ferromagnetic Tb: Experiment and theory, *Phys. Rev. B* **76**, 035123 (2007).
- [33] D. S. Inosov et al., Electronic Structure and Nesting-Driven Enhancement of the RKKY Interaction at the Magnetic Ordering Propagation Vector in Gd_2PdSi_3 and Tb_2PdSi_3 , *Phys. Rev. Lett.* **102**, 046401 (2009).
- [34] T. Nomoto, T. Koretsune, and R. Arita, Formation Mechanism of the Helical Q Structure in Gd-Based Skyrmion Materials, *Phys. Rev. Lett.* **125**, 117204 (2020).
- [35] M. A. Ruderman and C. Kittel, Indirect Exchange Coupling of Nuclear Magnetic Moments by Conduction Electrons, *Phys. Rev.* **96**, 99 (1954).
- [36] T. Kasuya, A Theory of Metallic Ferro- and Antiferromagnetism on Zener's Model, *Progress of Theoretical Physics* **16**, 45 (1956).
- [37] K. Yosida, Magnetic Properties of Cu-Mn Alloys, *Phys. Rev.* **106**, 893 (1957).
- [38] I. D. Hughes, M. Däne, A. Ernst, W. Hergert, M. Lüders, J. Poulter, J. B. Staunton, A. Svane, Z. Szotek, and W. M. Temmerman, Lanthanide contraction and magnetism in the heavy rare earth elements, *Nature* **446**, 650 (2007).
- [39] K. M. Döbrich, A. Bostwick, J. L. McChesney, K. Rossnagel, E. Rotenberg, and G. Kaindl, Fermi-Surface Topology and Helical Antiferromagnetism in Heavy Lanthanide Metals, *Phys. Rev. Lett.* **104**, 246401 (2010).

- [40] B. R. Ortiz et al., Evolution of Highly Anisotropic Magnetism in the Titanium-Based Kagome Metals LnTi_3Bi_4 (Ln: La \cdots Gd $^{3+}$, Eu $^{2+}$, Yb $^{2+}$), *Chem. Mater.* **35**, 9756 (2023).
- [41] Y. Hu et al., Real-space observation of incommensurate spin density wave and coexisting charge density wave on Cr (001) surface, *Nat Commun* **13**, 445 (2022).
- [42] Y. Liu et al., Superconductivity under pressure in a chromium-based kagome metal, *Nature* **632**, 1032 (2024).
- [43] J. O'Donnell, M. S. Rzchowski, J. N. Eckstein, and I. Bozovic, Magnetoelastic coupling and magnetic anisotropy in $\text{La}_{0.67}\text{Ca}_{0.33}\text{MnO}_3$ films, *Applied Physics Letters* **72**, 1775 (1998).
- [44] S. Jiang, H. Xie, J. Shan, and K. F. Mak, Exchange magnetostriction in two-dimensional antiferromagnets, *Nat. Mater.* **19**, 1295 (2020).
- [45] G. Kresse and J. Furthmüller, Efficiency of ab-initio total energy calculations for metals and semiconductors using a plane-wave basis set, *Computational Materials Science* **6**, 15 (1996).
- [46] J. P. Perdew, K. Burke, and M. Ernzerhof, Generalized Gradient Approximation Made Simple, *Phys. Rev. Lett.* **77**, 3865 (1996).
- [47] G. Pizzi et al., Wannier90 as a community code: new features and applications, *J. Phys.: Condens. Matter* **32**, 165902 (2020).

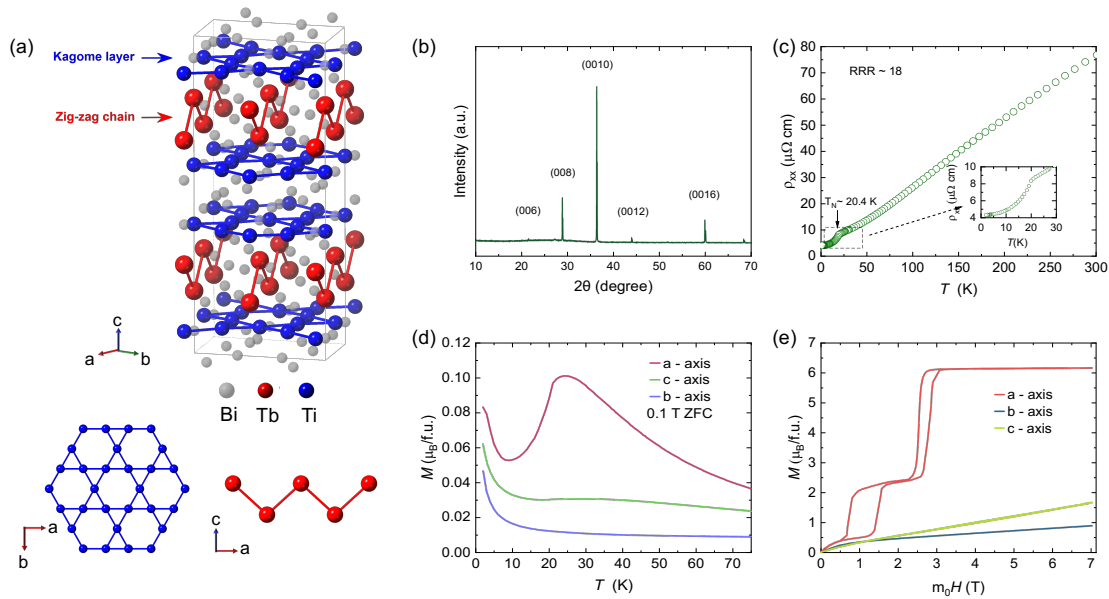


Fig. 1. Crystal structure and magnetism of TbTi_3Bi_4 . (a) Crystal structure of TbTi_3Bi_4 . The lower left and lower right panels show the kagome network and the intercalating zigzag chain of Tb, respectively. (b) The single crystal X-ray diffraction of TbTi_3Bi_4 . (c) The longitudinal electrical resistance along a -axis, showing the AFM transition at $\sim 20.4\text{ K}$. (d), (e) The temperature-dependent (d) and the field-dependent (e) magnetization along a -, b - and c -axes of the TbTi_3Bi_4 .

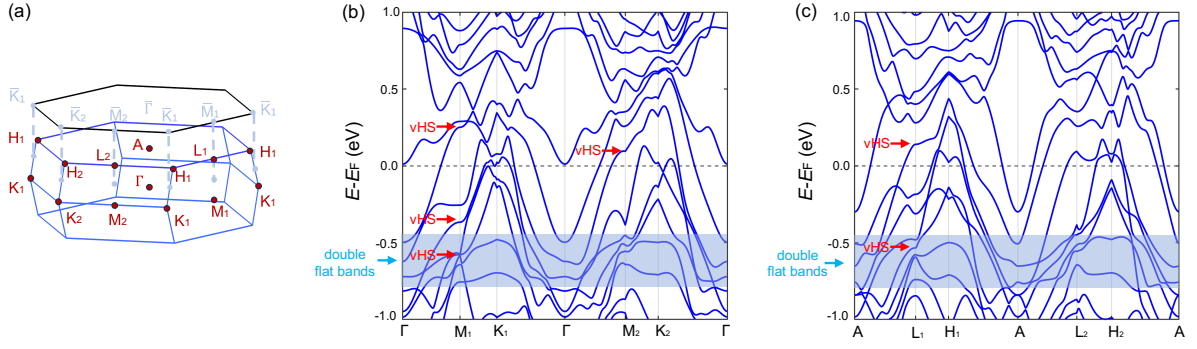


Fig. 2. The DFT calculation of the normal state. (a) Three-dimensional bulk BZ of TbTi_3Bi_4 (blue) and (001) projected surface BZ (black), with high symmetry points indicated. (b), (c) the DFT calculated band structure of non-magnetic bulk state along high symmetry line in $k_z = 0$ (b) and $k_z = \pi$ (c) plane, with kagome features (vHSs, flat bands) indicated.

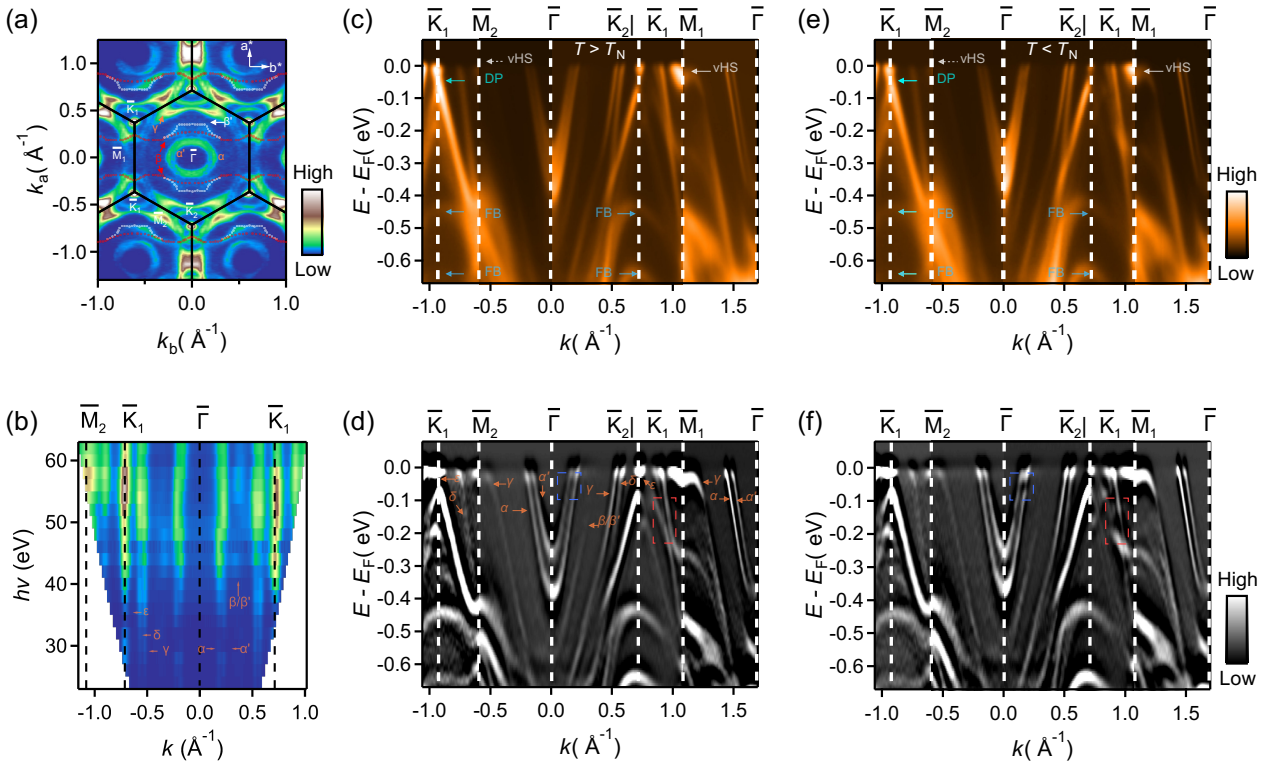


Fig. 3. The overall electronic structure of TbTi_3Bi_4 in the normal state and AFM state. (a) Fermi surface map of TbTi_3Bi_4 (using VUV light of LH, at 100 eV). The red and white dotted lines are guides for the eye indicating the quasi-1D bands. (b) Photon-energy-dependent constant energy map along \bar{M}_2 - \bar{K}_1 - $\bar{\Gamma}$ - \bar{K}_1 . (c), (d) Intensity (c) and the corresponding curvature plots (d) of the band structure along the high symmetry lines in the normal state. “DP” means Dirac point, and “FB” means flat band. (e), (f)

same as the (c) and (d), but taken in the AFM state. The blue dash rectangle and the red dashed rectangle in (d) and (f) indicate the band reconstruction.

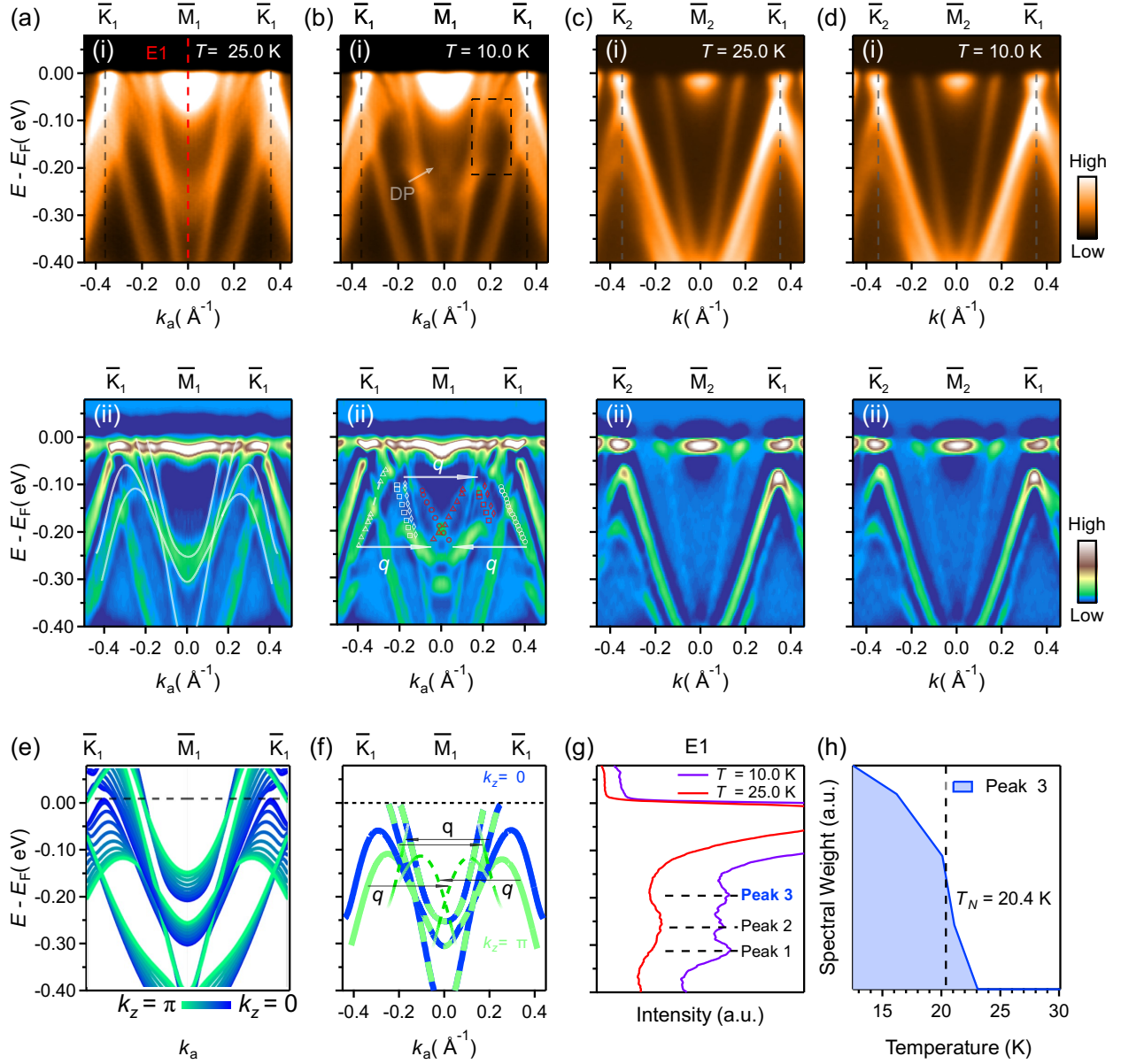


Fig. 4. Temperature dependence of the electronic band structure at \bar{M}_1 and \bar{M}_2 . (a) Intensity (i) and the corresponding curvature (ii) plots along \bar{K}_1 - \bar{M}_1 - \bar{K}_1 direction in the normal state ($T = 25.0$ K). E1 indicates the EDC at \bar{M}_1 , and the comparison with the EDC at \bar{M}_1 in AFM state is shown in Fig. 4(g). (b) Same as (a), but taken in the AFM state ($T = 10.0$ K). The black dashed rectangle in (i) highlights the DOS suppression. “DP” in (i) represents the Dirac point. Red marks in (ii) indicate the folding bands, and white marks in (ii) are the respective original bands. The white arrow indicates the folding vector q . (c), (d) Same as (a) and (b), but taken along \bar{K}_2 - \bar{M}_2 - \bar{K}_1 direction. (e) DFT calculation of k_z -projected band structure along \bar{K}_1 - \bar{M}_1 - \bar{K}_1 in the normal state. (f) Band dispersion extracted from (a), thick green and blue lines represent $k_z = \pi$ and $k_z = 0$ bands, respectively. Green dashed lines represent folding bands. (g) Energy distribution curves (EDCs) taken from \bar{M}_1 (indicated by E1) in the intensity plots of (a) and (b). Peak 3 represents the Dirac crossing point. (h) Temperature evolution of the spectral weight of Peak 3, data processing details are described in Appendix D.

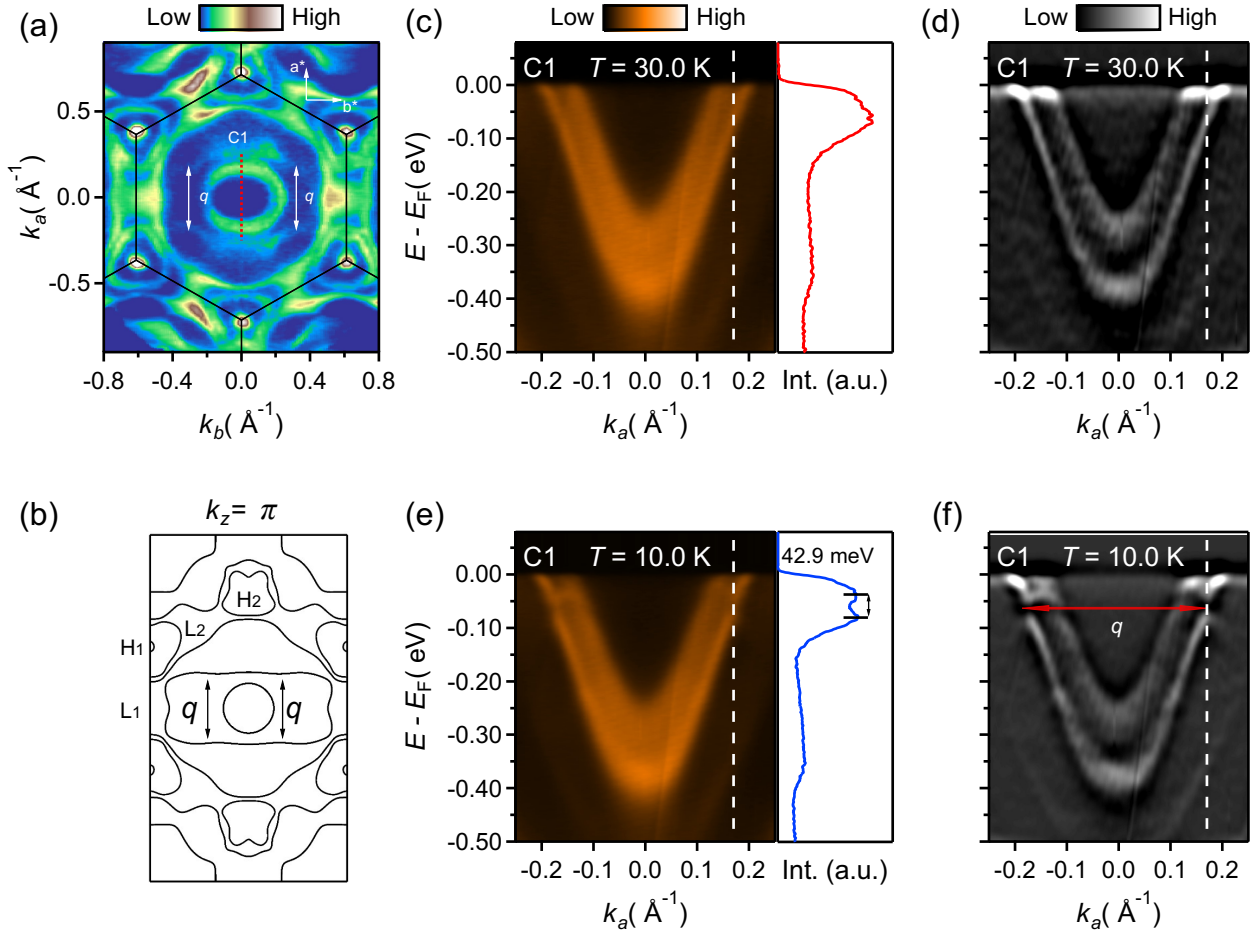


Fig. 5. Band folding around $\bar{\Gamma}$ point. (a) Fermi surface map taken with photons of LV+LH at 60 eV, with the red dashed line indicating the momentum location of cut C1 shown in (c)-(f), white arrows represent nesting vector connecting two branches of quasi-1D Fermi surface. (b) DFT calculated Fermi surface in the $k_z = \pi$ plane. (c), (d) Intensity (c) and the corresponding curvature (d) plots of α/α' pockets ($T = 30.0$ K) taken along C1 [red line in (a)]. EDC at the white dash line is present in the right panel of (c). (e), (f) Same as (c) and (d), but taken at $T = 10.0$ K. Gap opening (~ 42.9 meV) is visualized in the EDC shown in the right panel of (e).

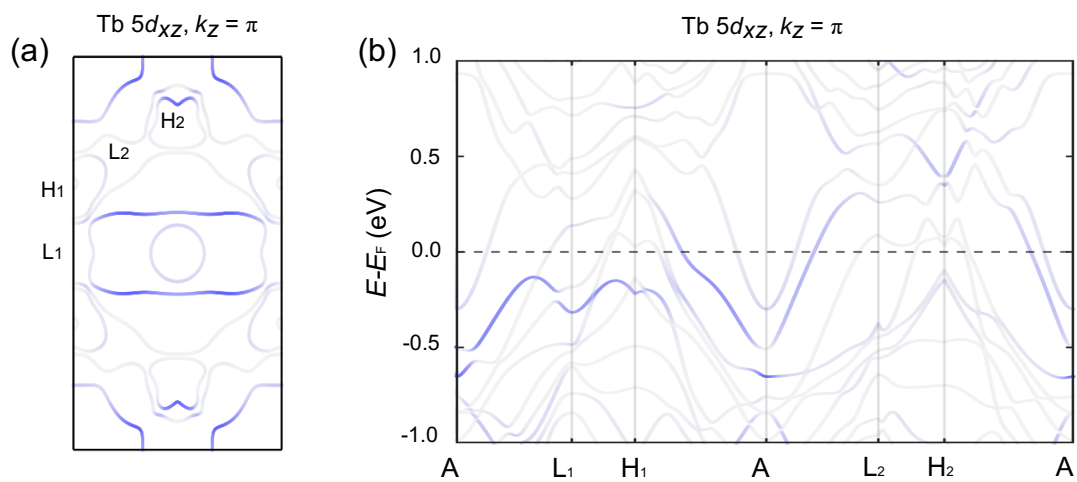


Fig. 6. DFT calculated orbital distribution of Tb- $5d_{xz}$. (a) DFT calculated orbital distribution of Tb- $5d_{xz}$ along the Fermi surface in the $k_z = \pi$ plane. (b) DFT calculated orbital distribution of Tb- $5d_{xz}$ in the energy band in the $k_z = \pi$ plane.

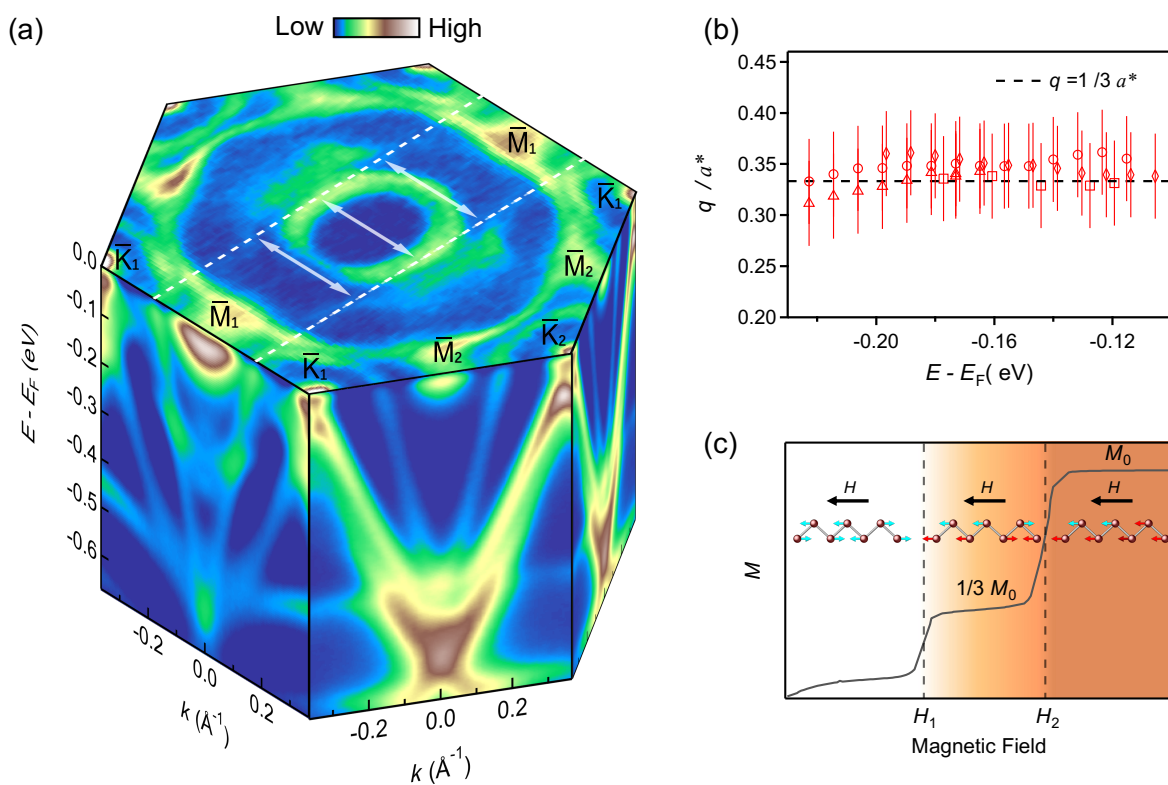


Fig. 7. Summary of electronic and magnetic properties of TbTi_3Bi_4 . (a) Anisotropic electronic structure and reconstruction in the AFM state. White arrows indicate the nesting vector. The obvious anisotropic reconstruction is clearly visualized on the side surfaces of \bar{M}_1 , and on the contrary, \bar{M}_2 does not show observable changes in the AFM state. (b) all the q -vectors taken from Fig. 4(d) and Fig. 5(f), these vectors are approximately around $1/3 a^*$, the error bar is estimated from the FWHM of the Dirac point in Fig. 4(b). (c) schematic of the mechanism of $1/3$ fractional magnetization plateau based on $3a$ AFM state (intralayer coupling larger than interlayer coupling). Red colored arrows indicate the flipped spin, dark red arrows represent the spin flipped twice. H_1 and H_2 indicate the magnetic field of metamagnetic transition.